AGU ADVANCING EARTH AND SPACE SCIENCES

Geophysical Research Letters

RESEARCH LETTER
10.1029/2024GL110430

# Could Developing Frontal Rainfall Influence Warm-Sector Rainfall?

**Hongpei Yang**[1,2,3], **Yu Du**[1,2,3], **Zijian Chen**[1,2,3], and **Junying Fang**[4]

[1]School of Atmospheric Sciences, Sun Yat-Sen University, and Southern Marine Science and Engineering Guangdong Laboratory (Zhuhai), Zhuhai, China, [2]Guangdong Province Key Laboratory for Climate Change and Natural Disaster Studies, Sun Yat-Sen University, Zhuhai, China, [3]Key Laboratory of Tropical Atmosphere-Ocean System, Sun Yat-Sen University, Ministry of Education, Zhuhai, China, [4]Institute of Tropical and Marine Meteorology, China Meteorological Administration, Guangzhou, China

**Abstract** Forecasting warm-sector rainfall (WR) remains a major challenge, primarily due to weak synoptic forcing. Through cloud-permitting numerical simulations, in addition to direct triggering mechanism from low-level jets, we identify the important role of gravity waves in a heavy WR event in South China via convective preconditioning. The preconditioning manifests as mid-level moistening and destabilization with wave-like variations. This process is driven by fast-propagating (~24 m $s^{-1}$) $n = 2$ waves, associated with lower-tropospheric ascents and upper-tropospheric descents. Waves are generated during the evolution of northern frontal rainfall (FR). As FR intensifies, surges in low-level diabatic cooling mainly resulting from microphysical processes, trigger $n = 2$ waves, which further precondition the environment along their path. In contrast, a sensitivity experiment involving stably developing FR fails to reproduce the preconditioning process by waves and the subsequent occurrence of WR. Overall, our study illuminates a new pathway through which FR significantly influences WR via gravity waves.

**Plain Language Summary** During the rainy season, the coastal regions of South China frequently experience heavy rainfall, leading to significant socio-economic losses. Unfortunately, understanding the mechanisms underlying this heavy rainfall and accurately predicting it remains a great challenge, as it often occurs without evident synoptic influences such as fronts and low-pressure vortex. Another rainband occasionally forms to the north of the coastal heavy rainfall through frontal lifting. The northern inland frontal rainfall could be considered a potential contributor to the initiation of coastal heavy rainfall, yet no concrete connection has been established until now. Our research reveals that this frontal rainband can generate low-frequency gravity waves that have a substantial influence on coastal heavy rainfall. These waves primarily result from the sharp cooling associated with the frontal rainband, featuring lower-tropospheric upward motions. They are capable to travel considerable distances ahead of the frontal rainband at high speeds. Along their journey, they moisten and destabilize the cloud environment ahead of the frontal rainband, thereby favoring the occurrence of coastal rainfall.

**Key Points:**

- The initiation of warm-sector heavy rainfall at the coast is related to the evolution of northern frontal rainfall that located 300 km away
- Variations in latent cooling resulting from the frontal rainfall produce gravity waves featuring ascents over the lower troposphere
- These gravity waves moisten and destabilize mid-level environment along their paths, promoting warm-sector rainfall

**Supporting Information:**

Supporting Information may be found in the online version of this article.

**Correspondence to:**

Y. Du,
duyu7@mail.sysu.edu.cn

**Citation:**

Yang, H., Du, Y., Chen, Z., & Fang, J. (2024). Could developing frontal rainfall influence warm-sector rainfall? *Geophysical Research Letters*, *51*, e2024GL110430. https://doi.org/10.1029/2024GL110430

Received 22 NOV 2023
Accepted 20 JUL 2024

**Author Contributions:**

**Conceptualization:** Yu Du
**Formal analysis:** Hongpei Yang, Yu Du
**Funding acquisition:** Yu Du, Junying Fang
**Investigation:** Hongpei Yang, Yu Du
**Methodology:** Hongpei Yang, Yu Du, Zijian Chen
**Project administration:** Yu Du
**Software:** Hongpei Yang, Zijian Chen
**Supervision:** Yu Du
**Validation:** Hongpei Yang
**Visualization:** Hongpei Yang, Junying Fang
**Writing – original draft:** Hongpei Yang
**Writing – review & editing:** Hongpei Yang, Yu Du, Zijian Chen, Junying Fang



## 1. Introduction

Two types of rainfall, namely frontal rainfall (FR) and warm-sector rainfall (WR), often co-occur in South China during the pre-summer rainy season (Liu et al., 2020; Zeng et al., 2023). FR and WR can both produce intense rainfall, resulting in severe flooding, economic losses and casualties. FR typically occurs in close proximity to the synoptic frontal zone, where the northern cold and dry air converges with southerly moist and warm airflow (Ding, 1994). In contrast, WR locates approximately 200–300 km away from significant synoptic-scale forcing, either in the warm-sector ahead of the surface front or within the southwesterly moist flow without any fronts nearby (Ding, 1994; S. Huang, 1986; Luo et al., 2017). A considerable proportion of FR events are accompanied by prefrontal convection, which may subsequently develop into WR events (Zeng et al., 2023). This coexistence of FR and WR has been confirmed through numerous case studies (e.g., Du, Chen, Han & Bai et al., 2020; Du, Chen, Han & Mai et al., 2020; Du & Chen, 2019, hereafter DC19; Han et al., 2021; Liu et al., 2020).

In contrast to FR that is associated with significant synoptic forcing, the forecast of WR remains a great challenge (L. Huang & Luo, 2017; Wang et al., 2014). The convection initiation (CI) of WR is impacted by a multitude of factors at various scales, including local convergence arising from low-level jets (e.g., Du & Chen, 2018, 2019; Du, Chen, Han & Bai et al., 2020; Du, Chen, Han & Mai et al., 2020; Zhang & Meng, 2019), land-sea contrast

(e.g., Chen et al., 2016; Gao et al., 2022), urban heating (e.g., Sun et al., 2021), orographic lifting (e.g., Bai et al., 2021; Wang et al., 2014) and cold pools (Wang et al., 2014; M. Wu & Luo, 2016), as well as their interactions (Du, Chen, Han & Bai et al., 2020; Su et al., 2023; M. Zhang et al., 2022; S. Zhang et al., 2022). Additionally, WR benefits from synoptic-scale ascent provided by upper-level jet streaks and warm-moist monsoon flow (Zeng et al., 2023). Interestingly, WR frequently occurs several hundred kilometers ahead of frontal rainfall with a time lag of a few hours (Du & Chen, 2019; Du, Chen, Han & Mai et al., 2020), but the front itself rarely triggers WR, one interesting question arises: apart from these known forcings, can FR itself influence WR?

One typical case occurred on May 10, 2014, where these two distinct types of rainfall coexisted, with WR producing extreme rainfall exceeding 200 mm in a day (Luo et al., 2017), reaching approximately 10% of the local annual average precipitation. Previous investigation by DC19 revealed that, in addition to the cooperation of two types of low-level jets (boundary layer jet, BLJ and synoptic low-level jet, SLLJ) that provides mesoscale lifting for WR, a significant mid-level moistening process before CI was also crucial in this case. Both sounding observations and numerical simulations showed that this moistening occurred at a higher altitude (750–600 hPa) and was accompanied by a substantial increase in convective available potential energy (CAPE) (their Fig.8, DC19). Such mid-level preconditioning processes cannot be fully explained by the known mechanisms, such as low-level jets and orographic lifting, as they generally occur at lower altitudes (e.g., surface–850 hPa).

One potential mechanism at play is the generation and propagation of gravity waves from FR. Convection in FR can produce low-frequency gravity waves as a result of microphysical heating and nonlinear motions (Adams-Selin, 2020a; Lane & Reeder, 2001; Yang et al., 2023). These waves are characterized by their respective $n$th vertical modes in the diabatic heating profile (Du et al., 2024; Mapes, 1993; Nicholls et al., 1991). For example, $n = 2$ waves exhibit upward motions in the lower troposphere and downward motions in the upper troposphere, and their generation is linked to processes such as raindrop evaporation, ice particles melting and sublimation (Adams-Selin, 2020a, 2020b; Groff et al., 2021). Given that the environment near the front tends to be stable, low-frequency waves have the capacity to propagate over considerable distances. These waves can influence the troposphere through two primary ways. When a ducting layer is present in the environment, waves with strong vertical motions exceeding 1–2 m $s^{-1}$ can directly trigger convection. However, even with relatively weak vertical motions, $n = 2$ waves humidify and destabilize the lower troposphere through adiabatic cooling and moistening (Adams-Selin, 2020a; Fovell, 2002; Lane & Reeder, 2001).

Therefore, gravity waves play an important role in CI, particularly for CI ahead of the mesoscale convective systems (MCS) at a distance (Adams-Selin, 2020a; Fovell et al., 2006; Groff et al., 2021). In this context, we hypothesize that FR may impact WR through the mediation of gravity waves, which has not been documented by previous studies regarding the formation mechanisms of WR. These waves might act as a preconditioning factor in the convective environment or provide an additional lifting mechanism. While previous studies have typically treated FR and WR separately, the aim of this study is to establish a causal relationship between these two distinct types of heavy rainfall in South China, providing new insights for improved WR forecasting.

## 2. Case Overview and Model Configuration

### 2.1. Case Overview

Based on the Climate Prediction Center morphing technique (CMORPH) rainfall data (Xie et al., 2018), an episode of WR was observed ahead of the inland FR over South China on 10 May 2014 (Figure 1a). The warm-sector convection of interest initiated around midnight (~1800 UTC, LST = UTC+8) along the coast and subsequently developed into a heavy WR event (Figure S1 in Supporting Information S1). While an earlier convection to the east of the CI location gradually decayed over time, its impact on the subsequent CI was limited, as discussed in DC19. The synoptic background analysis with the National Centers for Environmental Prediction Final (FNL) Operational Global Analysis data is illustrated in Figure S2 in Supporting Information S1. By 1800 UTC, 500 hPa westerlies were located over the South China, with northwesterly winds at higher latitudes continually guided the southward movement of cold air. This resulted in a surface high-pressure and the enhancement of cold front. The generation of FR ensued from the convergence of cold and warm air. In contrast, CI was situated on the warm side of the cold front. In this scenario, CI was dynamically favored by the approaching cold front (shear line accompanied by SLLJ at 700 hPa) and the nocturnal enhancement of the BLJ. CI was identified at the BLJ's terminus, characterized by convergence and the entrance of SLLJ, providing

10.1029/2024GL110430

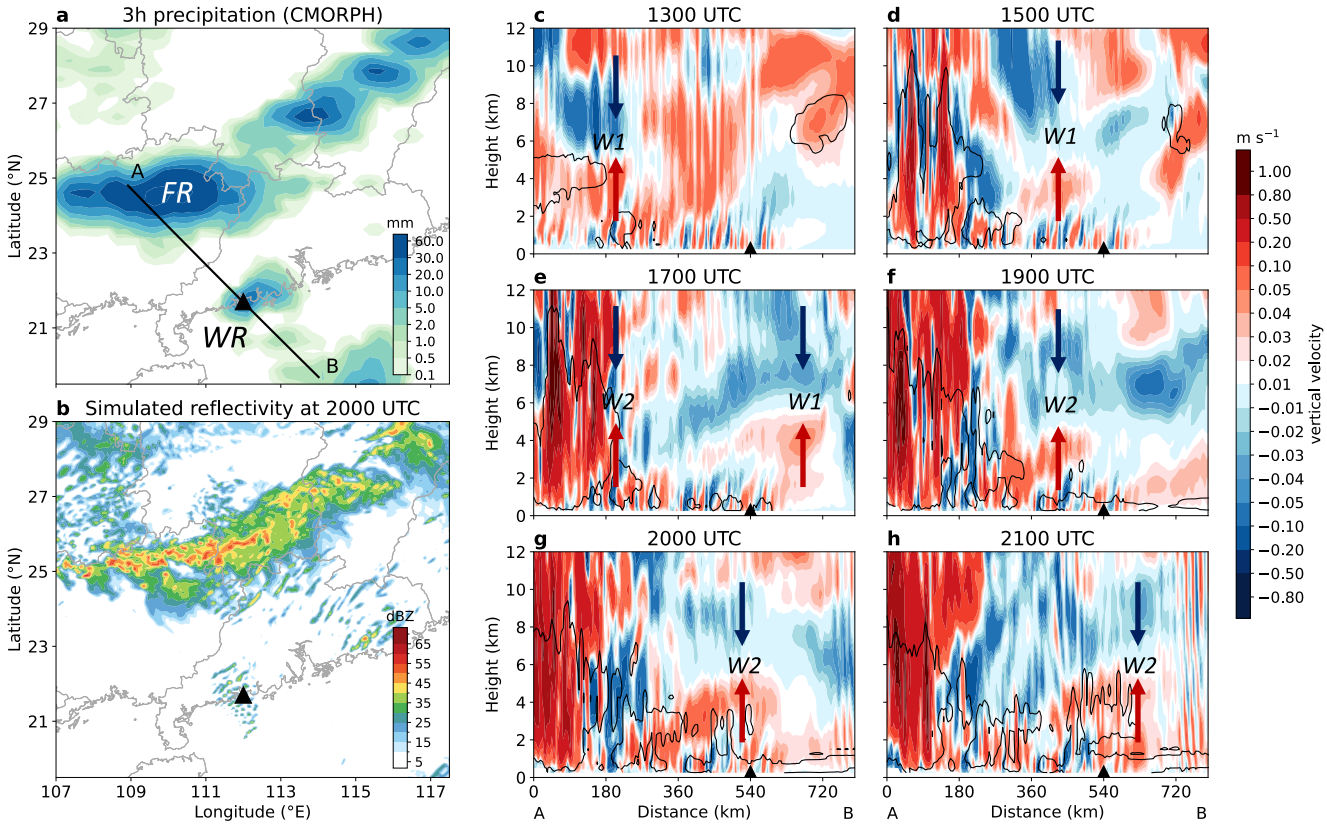


**Figure 1.** Southeastward propagating gravity waves ahead of the frontal rainfall. (a) 3 h (1800–2000 UTC, 10 May 2014) accumulated precipitation (mm) from CMORPH with frontal rainfall and warm-sector rainfall labeled by "FR" and "WR," respectively. The black line AB is used for cross sections in (c–h). (b) Simulated radar composite reflectivity (dBZ) from WRF at 2000 UTC. Vertical cross sections of vertical velocity (shaded, m $s^{-1}$) and cloud water mixing ratio (contour, 0.01 g $kg^{-1}$) at (c) 1300, (d) 1500, (e) 1700, (f) 1900, (g) 2000 and (h) 2100 UTC. Two $n = 2$ gravity wave couplets propagating ahead of the frontal rainfall are marked by arrows (W1 and W2). The black triangles denote the CI location of WR.

divergence (DC19). Therefore, despite the presence of significant CIN in the near-surface layers (Figure S1e in Supporting Information S1), the necessary mesoscale lifting for elevated convective development was provided. In addition to double low-level jets, coastal terrain and land breeze may also play roles in determining the location of CI and aiding in producing heavy rainfall (e.g., Chen et al., 2016). The subsequent section will investigate the rapid midlevel (~650 hPa) moistening process that responsible for CI and its relationship with FR and gravity waves.

### 2.2. Numerical Model Setup and Validation

To explore the potential influences of FR on WR, we employed the Advanced Research version of the Weather Research and Forecasting (WRF-ARW) Model, version 4.0 (Skamarock et al., 2019) in this study. A one-way nested configuration with two domains (Figure S3 in Supporting Information S1) was used with 12-km and 4-km horizontal grid-spacing and 51 stretched vertical levels. Note that the inner domain encompassed both FR and WR, facilitating the analysis of gravity waves. Additionally, a 5-km gravity wave-absorbing layer was introduced near the model top at 50 hPa. Through multiple experiments, it was found that WR exhibited high sensitivity to initial conditions and could only be accurately reproduced when the simulation was initialized at 1200 UTC May 10 using FNL data (CTRL run). The Thompson et al. (2008) microphysics scheme was selected, providing latent heating rate output (Text S1 in Supporting Information S1). Various physical parameterizations were incorporated, including the Yonsei University planetary boundary layer scheme (Hong et al., 2006), the Rapid Radiative Transfer Model for Global Climate Models longwave and shortwave radiation scheme (Iacono et al., 2008), the revised MM5 Monin-Obukhov surface-layer scheme (Jiménez et al., 2012), and the unified Noah land-surface-model (Livneh et al., 2011). The Kain-Fritsch cumulus parameterization (Kain, 2004) was applied solely in the outer domain (d01).

Model performance was initially assessed, revealing that both FR and WR were well captured in the CTRL run (Figures 1a and 1b). As depicted in Figure S4 in Supporting Information S1, the location of FR with most intense precipitation aligned with that in CMORPH, slightly moving southward before CI. Although the simulated time of CI was approximately 2 hours delayed, the location of CI, and the atmospheric conditions closely matched the observations, indicating the successful reproduction of CI with associated mesoscale processes. Therefore, the CTRL run was suitable for investigating the intriguing relationship between FR and WR.

## 3. Preconditioning Processes Related to Gravity Waves for WR

To examine the potential influence of gravity waves on WR, we first plot the potential wave propagating path between FR and WR (line AB in Figure 1). Subsequently, a horizontal average of WRF outputs is performed within the range of 40 km on both sides of line AB to better represent the propagation of gravity waves. Figures 1c–1h show the presence of two vertical motions' dipoles, with ascents over the lower troposphere and descents over the upper troposphere, propagating in succession ahead of FR for more than 300 km. The Hovmöller diagrams highlight a pronounced shoreward propagation, whose speed is faster than the movement speed of FR, implying gravity waves (Figures 2a and 2b). The phase lag between variations in potential temperatures and vertical motions indicates $n = 2$ waves (Figures 2c and 2d). The existence of these $n = 2$ waves is further confirmed through an objective wave identification method — *Spectral Filtering* (Figure S5 in Supporting Information S1; Lane, 2021; Yang & Du, 2024). The fundamental concept of this method is to retain spectral components with vertical wavenumbers falling within the range of $n = 2$ waves and subsequently reconstructing vertical motions field through inverse Fourier transformation. Detailed information on this method is given in Text S2 in Supporting Information S1. Examinations and identifications were also performed on other wave modes (e.g., $n = 1, 3$ waves), but their signals are less pronounced (not shown), indicating their minimal impacts in this case. Therefore, our focus is on $n = 2$ waves, particularly those branches associated with lower-tropospheric ascents and upper-tropospheric decents (dot-dashed lines in Figures 2c and 2d).

Estimates of wave phase speeds along line AB, derived from the slope of black lines in Figure 2a, suggest a speed of approximately 24.0 m $s^{-1}$. Theoretical calculation, based on the hydrostatic dispersion relationship, indicates that the horizontal wave phase speed ($c$) is determined by

$$c = \frac{ND}{n\pi} + \overline{u},$$

where $D$ is the depth of the vertical distance between the top of the heating layer and the bottom of the cooling layer in deep convection, and $N$ and $\overline{u}$ are the averaged tropospheric Brunt–Väisälä frequency and the speed of projected horizontal winds along wave path, respectively (Nicholls et al., 1991). Figure S6a in Supporting Information S1 demonstrates a vertically averaged wind profile with a weak v-wind (nearly zero) and moderate westerly (~8.8 m $s^{-1}$) along the wave path over land. Consequently, the wind speed along the path, at a 45° angle to the meridional direction, is approximately 6.2 m $s^{-1}$. The mean environmental buoyancy frequency $N$ is relatively large with a value of $1.21 \times 10^4$ $s^{-1}$ due to the deep stable layer ahead of FR (Figure S6b in Supporting Information S1). In such an environment, $n = 2$ waves would have a speed of 27.4 m $s^{-1}$ assuming $D$ approximates the distance between surface and tropopause (~11 km). Hence, the simulated wave speed aligns well with theoretical values.

After the passage of the second $n = 2$ waves at around 2000 UTC, CI occurs at the coast (Figures 1g and 2a). The mid-level environment is found to be moistened before CI, and cloud water generally develops above 2 km, rather than from the surface (Figure S7 in Supporting Information S1). Although the nocturnal enhancing BLJ transports water vapor from the South China sea, the jet-related moistening effect is located at a lower altitude (below 1 km) and features onshore strengthening. However, as shown in Figure 2e, the change in mid-level relative humidity and water vapor exhibits significant offshore enhancement. A similar phenomenon is observed in the variation of CAPE and CIN (Figure 2f). This enhancement in the mid-level cloud environment is induced by waves. These $n = 2$ waves produce positive displacements for air parcels in the lower troposphere and negative displacements in the upper troposphere, cooling and moistening lower atmosphere, resulting in an increase in CAPE and a decrease in CIN (Lane & Reeder, 2001). Since $n = 2$ waves have the largest amplitudes at an altitude of 2–4 km, wave-related preconditioning processes are most significant at the mid-level. It is essential to note that waves may not directly initiate convection in this scenario, as their magnitude is relatively small on an order of 0.1 m $s^{-1}$

10.1029/2024GL110430



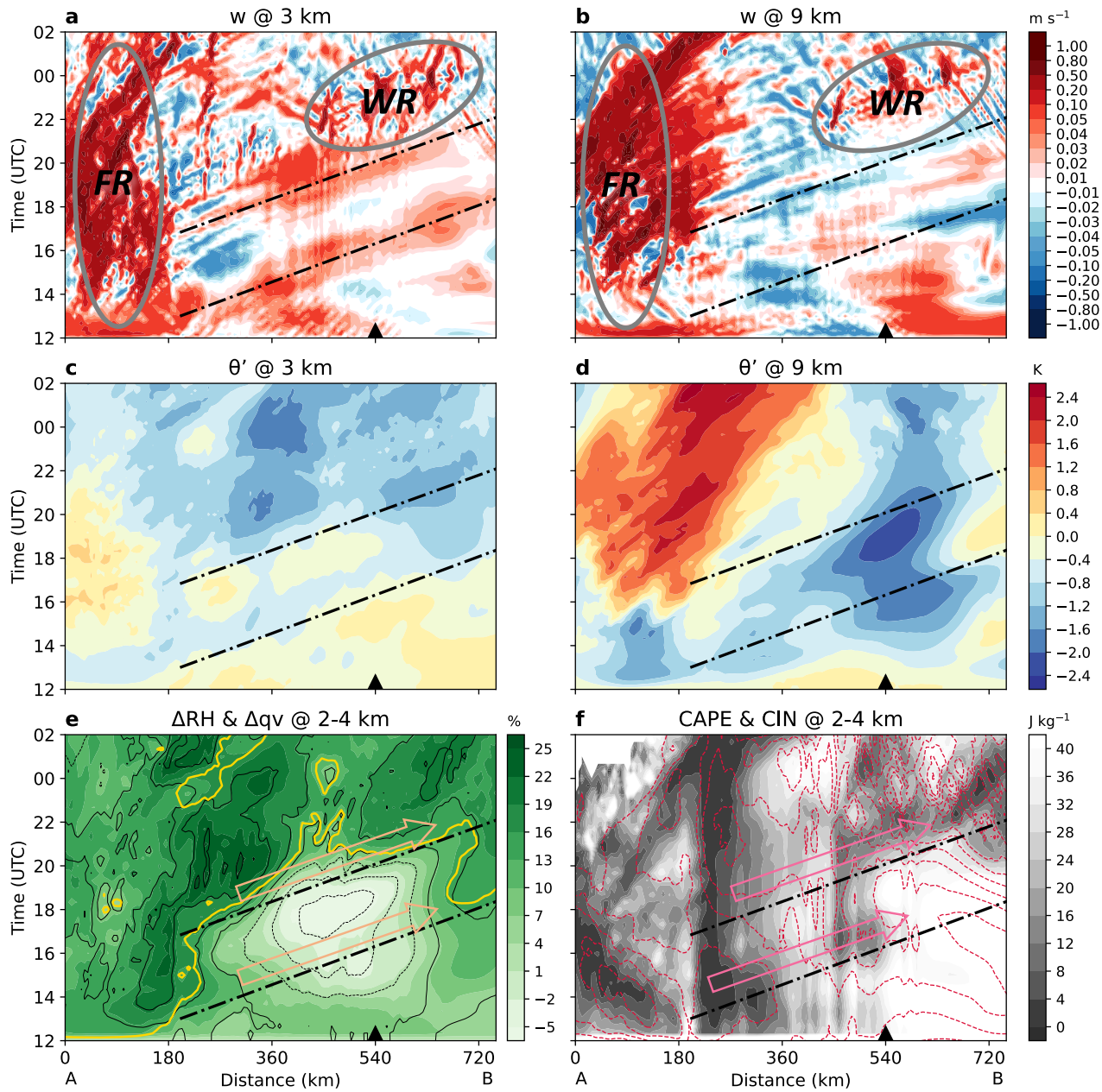


**Figure 2.** Polarization relationship of gravity waves and their environmental response. Time-distance Hovmöller diagrams of vertical motions (m $s^{-1}$) at (a) 3 km and (b) 9 km AGL, perturbation potential temperatures (K) at (c) 3 km and (d) 9 km AGL, (e) the changes in relative humidity (shaded, %) and water vapor mixing ratio (contoured from −5 to 5 g $kg^{-1}$ at an interval of 0.5 g $kg^{-1}$) relative to the state at 12 UTC averaged within 2–4 km AGL and (f) the convective available potential energy (CAPE, contoured in pink from 200 to 2,000 J $kg^{-1}$ at an interval of 200 J $kg^{-1}$) and convective inhibition (CIN, shaded, J $kg^{-1}$) averaged over 2–4 km AGL along the line AB in Figure 1b. Yellow contour in (e) denotes relative humidity larger than 90%, while black dash-dotted lines delineate $n = 2$ waves associated with low-level ascending motions and high-level descending motions. Orange arrows in (e) and pink arrows in (f) denote offshore enhancement in moisture and instability, respectively. Frontal rainfall (FR) and warm-sector rainfall (WR) are marked by ellipses in (a, b). The black triangles denote the CI location of WR.

(Figures 1g and 2a). However, their modifications to the environment are shown to be crucial in CI. Additionally, the preconditioning for WR is attributed to the cumulative effects of previously passed waves (W1 and W2). As shown in Figures 2e and 2f, the mid-level environment along the wave path is gradually humidified and destabilized after the propagation of W1. The environment is then dried partially due to the adiabatic warming and drying effect associated with the opposing $n = 2$ downward branch (Figure S5b in Supporting Information S1)

while the localized dry center near coast might be related to synoptic or mesoscale processes. Nevertheless, as the second $n = 2$ upward branch (W2) is generated and propagate southeastward, the cloud environment is revitalized, with mean relative humidity exceeding 90% (Figures 2e and 2f). With the arrangement of SLLJ and BLJ, CI is promoted at the coast (Figure S8a in Supporting Information S1).

Using the same FNL data, but with random perturbations on the initial stream function field of the outer domain via WRF data assimilation (CV3 option), a sensitivity experiment (RAND run) also successfully captured both FR and WR. However, WR occurs two hours earlier (1800 UTC) at the same location (Figure S9 in Supporting Information S1). Distance-time Hovmöller diagrams display that WR occurs immediately after the passage of W1 (Figures S10a and S10b in Supporting Information S1). A detailed comparison against W1 in the CTRL run reveals that W1 in the RAND run exhibits the same propagation speed but has a larger overall amplitude. Consequently, the mid-level environment is preconditioned to a greater extent, favoring an earlier CI. Mesoscale lifting by double LLJs is also noted in the RAND run, albeit slightly weaker than that in the CTRL run. Hence, in addition to mesoscale lifting by LLJs, gravity waves also play an important role in WR via preconditioning environment, prompting further investigation into their generation mechanism.

## 4. Generation of Gravity Waves From FR

This section examines how FR excite gravity waves, focusing on the generation of $n = 2$ waves primarily through stratiform-type heating profile. This profile consists of cooling in the lower half of the troposphere and heating aloft (Fovell, 2002; Lane & Reeder, 2001; Mapes, 1993; Nicholls et al., 1991). Figures 3a–3c exhibit potential temperatures associated with the development of the FR at 850 hPa. As FR develops, noticeable cooling appears behind it, intensifying over time. This enhancement of FR is also observed from radar reflectivity (Figures S1a–S1c in Supporting Information S1). Near the starting point $A$ (108.9°E, 24.8°N) of wave path in Figures 1a and 1b, a local strong cooling center rapidly evolves, with the low-level air experiencing a drop of more than −4 K in potential temperature within 5 hours (Figure 3c). To assess the heating profile, a spatiotemporal averaging of local heating rate ($\partial\theta'/\partial t$) over the cooling center (orange box in Figures 3a–3c) before CI (1200–1900 UTC) is conducted. Figure 3d shows that the mean heating profile generally features heating in the upper half of the troposphere and cooling over the lower half. Additionally, the strongest cooling at roughly 1 km AGL is nearly twice the magnitude of upper heating. This heating profile, coupled with the enhancement of low-level cooling before CI, is conducive to the generation of $n = 2$ waves.

In response to the atmospheric imbalance (Yang et al., 2023), the generation of gravity waves is closely connected to the changes in the diabatic heating profile. A surge in latent cooling or a significant enhancement of nonlinear motions can disturb stable air, leading to wave excitation. Vertical Fourier decomposition is performed on the local heating rate changes $M(z,t)$ to examine the relationship between FR development and the identified two $n = 2$ waves. Similar to Adams-Selin (2020a) and Stephan et al. (2016), $M(z,t)$ is decomposed into different heating modes using the formula

$$M(z,t) = \sum_{n=1}^{\infty} F_n(t) \sin \frac{\pi n z}{D}$$

where $F_n$ is the coefficient of each Fourier component, $z$ is the height, and the first 10 components ($F_1$–$F_{10}$) are calculated. Since $n = 2$ waves are the focus of this study, only $F_2$ is plotted in Figure 3e. As shown in Figure 2, the first $n = 2$ wave with upward motions in the lower troposphere is generated at around 1330 UTC, while the second $n = 2$ wave first appears approximately at 1700 UTC ahead of the FR. Unlike MCSs with strong vertical motions and latent heat release, the development of FR is more stable and the front-associated buoyancy flow is gentler, resulting in a minor contribution of nonlinear advection (not shown). Therefore, the focus here is on identifying essential microphysical processes accounting for wave generation.

At 1330 UTC, coefficient $F_2$ reaches its local minimum, indicating an increase in low-level cooling (Figure 3e). This is attributed to the formation of the western FR, as the location of strongest cooling aligns with where hourly precipitation exceeds 5 mm (Figure 3a). The evaporation of rainfall contributes significantly to the excitation of W1 (Figure 3e). Since the vertical motion of frontal convection is generally weak (Figure 2a), warm rain processes might dominate during this period. However, about 3–4 hours later, the western part of FR strengthens, more regions are influenced by the rainband (Figure 3c), and the cloud top reaches 11 km AGL (Figure 1e). More

10.1029/2024GL110430

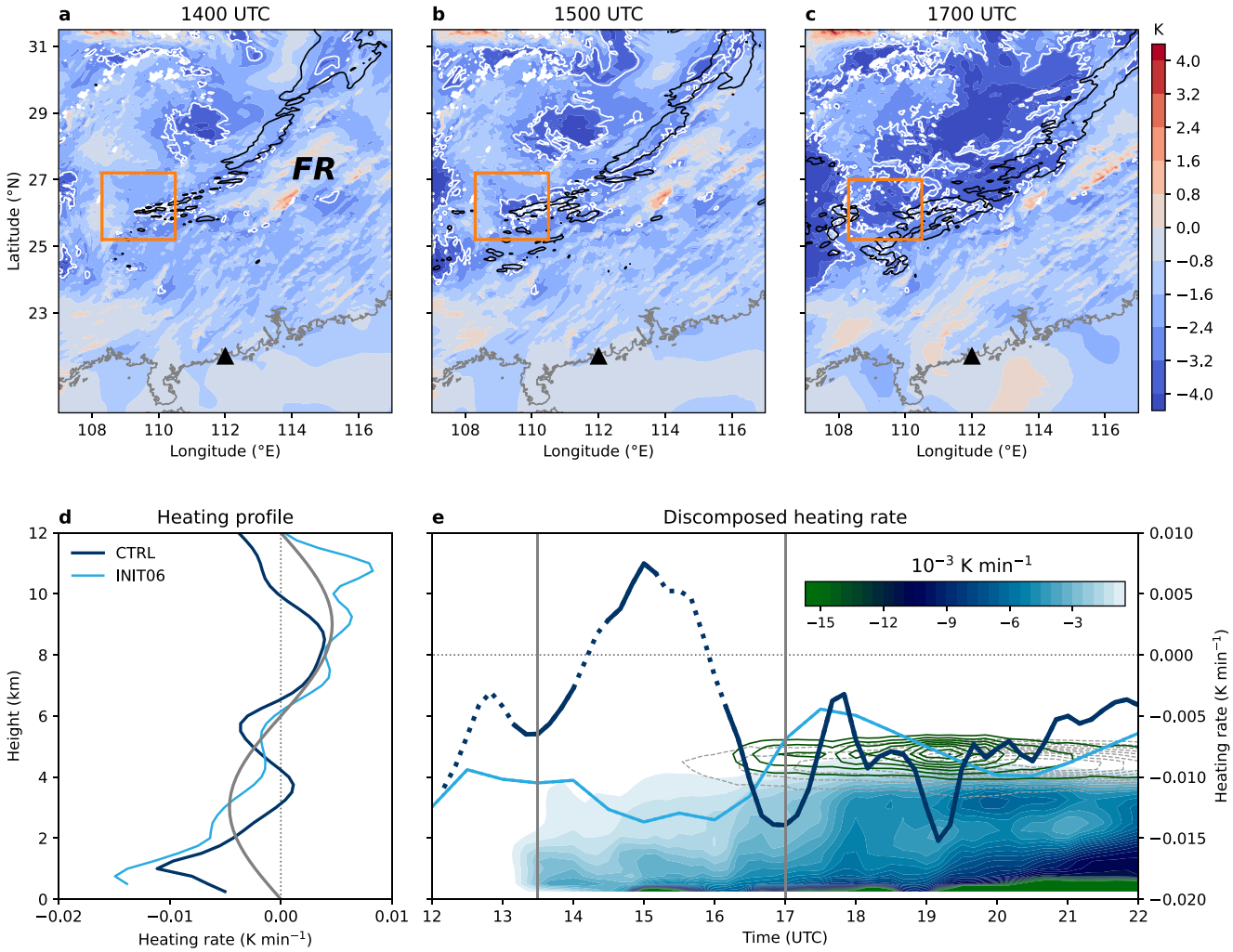


**Figure 3.** Generation of two $n = 2$ gravity waves from frontal rainfall (FR). Horizontal distribution of simulated 850 hPa perturbation potential temperatures (shaded, K; white contour, -3K) and hourly precipitation (black contour, 5 mm) at (a) 1400, (b) 1500 and (c) 1700 UTC. Orange boxes in (a–c) denote the western cooling center developed behind FR, which are used in (d, e). (d) Temporal mean (1200–1900 UTC, before CI) and box-averaged vertical profile of local heating rate (K min$^{-1}$) for the CTRL (dark blue line) simulation and sensitivity experiment INIT06 (light blue line). Gray solid line represents an idealized heating profile for $n = 2$ waves. (e) Time-height diagram of cooling tendencies from evaporation (shaded, K min$^{-1}$), melting (green contours at an interval of 0.002 K min$^{-1}$) and sublimation (gray dotted contours at an interval of 0.002 K min$^{-1}$) averaged over the box region from the CTRL run. Overlaid are $n = 2$ coefficients $F_2$ (dark blue line for the CTRL run, light blue line for the INIT06 run) derived by the Fourier vertical decomposition of local heating rate, which are plotted in solid line only if they are significant at a 95% significance level according to the two-tailed $t$ test. Generation time for the first and second $n = 2$ wave is marked by gray vertical lines. The right axis labels in (e) correspond to the values of the $n = 2$ coefficients. The black triangles denote the CI location of WR.

water vapor is ingested and transported upward to form ice particles. Then melting and sublimation of ice particles, along with evaporative hydrometeors, lead to another surge in low-level cooling at 1700 UTC (Figure 3e). This is evident in the variation in coefficient $F_2$, exhibiting a significant local minimum, indicating the generation of W2. Additionally, the generation of the opposing branch of $n = 2$ wave featuring lower-tropospheric downdraft and upper-tropospheric updraft, is attributed to the positive local heating rate at around 1500 UTC (Figure 3e). In comparison to observations, we also found an approximately 2-hours delayed evolution of the simulated FR (not shown), possibly explaining why CI was postponed 2 hours in the simulation. Hence, these results demonstrate that FR can excite low-frequency waves during its evolution, which can travel long distances to impact WR.

Another sensitivity experiment with the initial and boundary condition initialized 6 hours earlier (0600 UTC 10 May, INIT06), however, failed to reproduce WR. In a detailed comparison with the results from the CTRL run, we investigated the reasons behind this failure. Our initial focus was on whether the cooperation of two types LLJ was regenerated. Figure S8 in Supporting Information S1 indicates that the INIT06 run generally exhibits a similar

pattern of the BLJ and SLLJ near the coast, along with their associated divergence/convergence, compared to the CTRL run. Both simulations demonstrate evident mesoscale lifting exits at the coast before CI, albeit the mesoscale lifting in the INIT06 is slightly weaker. In generally, the INIT06 run captures the dynamic mechanism of WR. However, the wave-related preconditioning processes are missed in the INIT06 run. Wave signals ahead of the FR are not significant in the INIT06 run (Figure S10b in Supporting Information S1), leading to a lack of moistening and destabilizing of the mid-level air (Figures S10d and S10f in Supporting Information S1). Due to the relative drier environment (less than 90%, Figure S10b in Supporting Information S1), WR cannot occur even with mesoscale lifting. Hence, the CI failure could be partially attributed to the absence of waves, albeit other processes may also slightly vary in the INIT06.

Further investigation into absence of waves in the INIT06 run reveal that, although the spatiotemporal vertical heating profile is comparable to that of the CTRL run, the heating/cooling magnitude in the INIT06 run is slightly larger (light blue line in Figure 3d). However, the low-level environment in the INIT06 is continually cooled due to FR, with no clear surge in $F_2$ observed (Figure 3e). This persistent cooling may enhance the vertical motions along the front but not facilitate wave generation. Consequently, waves' propagation and their associated preconditioning processes are not included in the INIT06 run.

## 5. Conclusions

The present study represents the first comprehensive investigation into the underlying mechanisms through which frontal rainfall (FR) influences warm-sector rainfall (WR). Utilizing convection-permitting simulations, we discover the important role of gravity waves in connecting these two geographically separated rainbands. During the FR development, the coastal region, where WR originates, exhibits mid-level moistening and destabilization before convection initiation (CI). These preconditioning processes ahead of FR result from the FR development and are identified as essential for CI in WR. Figure 4 summarizes the key processes by which FR impacts WR through emitting gravity waves.

A northeast-southwest oriented cold front forms as the northerly cold airflow converges with the southerly warm-moist monsoon flow in South China. The FR forms in proximity to this front and undergoes a gradual evolution. During the FR's development, two distinct surges in low-level cooling, primarily arising from the evaporation, melting and sublimation of hydrometeors, occur at the western FR prior to WR. These low-level cooling episodes generate two $n = 2$ wave couplets characterized by ascents in the lower troposphere and descents in the upper troposphere. In a stable environment ahead of FR, these $n = 2$ waves propagate southeastward, perpendicular to the FR orientation, at a fast speed of approximately 24 m $s^{-1}$, considering the mean background wind along their path (~6.2 m $s^{-1}$). At this velocity, the waves can travel 300 km in less than 2 hours. While the amplitudes of FR-excited waves are generally modest and insufficient to directly trigger WR, their modification to the tropospheric environment is considered more important in this scenario. These waves effectively cool and moisten mid-level air, increasing environmental humidity and instability. Consequently, they favor convective development ahead of the FR. Along the path influenced by these waves, WR finally occurs where strong lifting is provided by the double low-level jets (SLLJ and BLJ). Therefore, FR exposes its influence on WR by improving convective environment through gravity waves.

In summary, this study reveals a close and robust relationship between FR and WR with gravity waves acting as a key connector. This study distinguishes from previous studies by introducing the remote impacts of FR, rather than focusing solely on the local forcings of WR. While this is a case study, a recent statistical analysis has demonstrated that over 66% of cold fronts in South China coincide with prefrontal convection (Zeng et al., 2023), encouraging further investigation into the extent of their correlation with waves excited by FR. Further exploration into the interaction among upstream factors (e.g., gravity waves and LLJs) and local factors (e.g., cold pool and topography) that contribute to WR, as well as their relative contributions, would deepen our understanding of WR dynamics. Furthermore, the predictability of WR remains low even in state-of-art convection-resolving models (L. Huang & Luo, 2017; N. Wu et al., 2020). With the incorporation of gravity waves and related FR convective processes, our study provides the foundation for improving WR forecasts by allowing a more accurate description of the evolution and location of FR. Potential methods include the assimilation of high spatial-temporal observations, such as radar data (Rao et al., 2023), radiosonde data (M. Zhang et al., 2022; S. Zhang et al., 2022), and all-sky geostationary satellite infrared radiance data (Y. Wu et al., 2020). Extensive

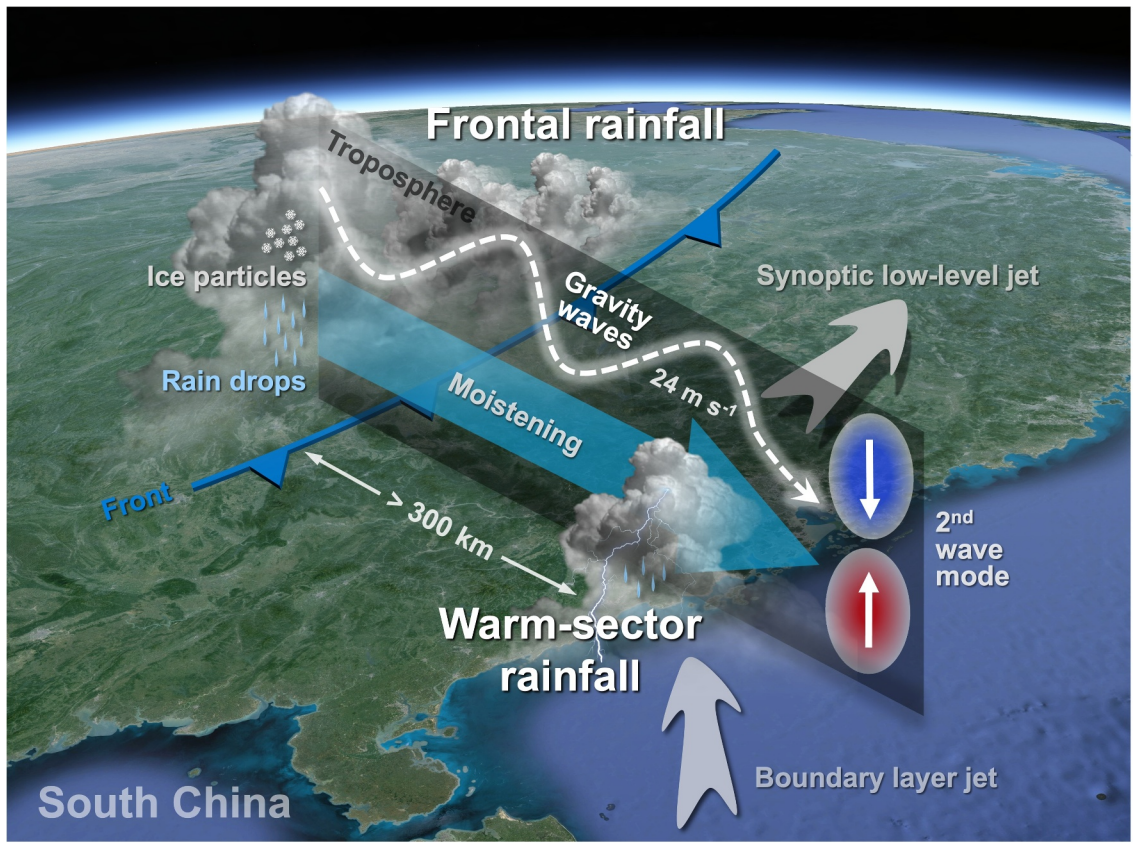


**Figure 4.** Conceptual model illustrating the mechanism by which FR influences WR through gravity waves. The low-level cooling, mainly driven by the microphysical cooling processes during the development of frontal rainfall, generates $n = 2$ gravity waves with ascending motions in the lower troposphere. Subsequently, these gravity waves propagate offshore at a fast speed, moistening and destabilizing the mid-level atmosphere ahead of the FR. Along their path, WR occurs at the coast, where strong mesoscale lifting is provided by the cooperation of the SLLJ and BLJ. Images/Maps data: Google Earth, TerraMetrics, Landsat/Copernicus, SIO, NOAA, U.S. Navy, NGA and GEBCO.

investigations to determine whether the relationship between FR and WR can be represented in regional climate models would also be of great value.

**Acknowledgments**

Thank you to Bin Han from GFDL for providing instructions regarding the microphysical heating rate calculation used to create Figure 3e. We also acknowledge the high-performance computing support from School of Atmospheric Science of Sun Yat-Sen University. This study was supported by the National Natural Science Foundation of China (No. 42122033), the Innovation Group Project of Southern Marine Science and Engineering Guangdong Laboratory (Zhuhai) (No. 316323005), the National Natural Science Foundation of China (No. 42075006), the Guangdong Major Project of Basic and Applied Basic Research (2020B0301030004), the Key Innovation Team of China Meteorological Administration (CMA2023ZD08), the Guangdong Basic and Applied Basic Research Foundation (2023A1515110811) and the Science and Technology Study Project of Guangdong Meteorological Bureau (GRMC2023Q34).

## Data Availability Statement

The FNL reanalysis data used in this study are available from the NCAR's Data Support Section at https://rda.ucar.edu/datasets/ds083.2/ (NCEP, 2000). The CMORPH satellite precipitation data are available from the National Oceanic and Atmospheric Administration Climate Prediction Center through ftp.cpc.ncep.noaa.gov/precip/CMORPH_V1.0/CRT (Xie et al., 2018). The WRF model data used for the figures and analysis are available at https://doi.org/10.5281/zenodo.10183294 (Yang, 2023).

## References

Adams-Selin, R. D. (2020a). Impact of convectively generated low-frequency gravity waves on evolution of mesoscale convective systems. *Journal of the Atmospheric Sciences*, *77*(10), 3441–3460. https://doi.org/10.1175/JAS-D-19-0250.1

Adams-Selin, R. D. (2020b). Sensitivity of MCS low-frequency gravity waves to microphysical variations. *Journal of the Atmospheric Sciences*, *77*(10), 3461–3477. https://doi.org/10.1175/JAS-D-19-0347.1

Bai, L., Chen, G., Huang, Y., & Meng, Z. (2021). Convection initiation at a coastal rainfall hotspot in South China: Synoptic patterns and orographic effects. *Journal of Geophysical Research: Atmospheres*, *126*(24), e2021JD034642. https://doi.org/10.1029/2021JD034642

Chen, X., Zhang, F., & Zhao, K. (2016). Diurnal variations of the land–sea breeze and its related precipitation over South China. *Journal of the Atmospheric Sciences*, *73*(12), 4793–4815. https://doi.org/10.1175/JAS-D-16-0106.1

Ding, Y. (1994). *Monsoons over China*. Kluwer Academic Publishers.

Du, Y., & Chen, G. (2018). Heavy rainfall associated with double low-level jets over southern China. Part I: Ensemble-based analysis. *Monthly Weather Review*, *146*(11), 3827–3844. https://doi.org/10.1175/MWR-D-18-0101.1

Du, Y., & Chen, G. (2019). Heavy rainfall associated with double low-level jets over southern China. Part II: Convection initiation. *Monthly Weather Review*, *147*(2), 543–565. https://doi.org/10.1175/MWR-D-18-0102.1

Du, Y., Chen, G., Han, B., Bai, L., & Li, M. (2020). Convection initiation and growth at the coast of South China. Part II: Effects of the terrain, coastline, and cold pools. *Monthly Weather Review*, *148*(9), 3871–3892. https://doi.org/10.1175/MWR-D-20-0090.1

Du, Y., Chen, G., Han, B., Mai, C., Bai, L., & Li, M. (2020). Convection initiation and growth at the coast of South China. Part I: Effect of the marine boundary layer jet. *Monthly Weather Review*, *148*(9), 3847–3869. https://doi.org/10.1175/MWR-D-20-0089.1

Du, Y., Rotunno, R., Chen, Z., & Yang, H. (2024). A linear theory for periodic convectively forced gravity waves near a coastline. *Journal of the Atmospheric Sciences*, *81*(7), 1271–1288. https://doi.org/10.1175/jas-d-23-0173.1

Fovell, R. G. (2002). Upstream influence of numerically simulated squall-line storms. *Quarterly Journal of the Royal Meteorological Society*, *128*(581), 893–912. https://doi.org/10.1256/0035900021643737

Fovell, R. G., Mullendore, G. L., & Kim, S.-H. (2006). Discrete propagation in numerically simulated nocturnal squall lines. *Monthly Weather Review*, *134*(12), 3735–3752. https://doi.org/10.1175/MWR3268.1

Gao, X., Luo, Y., Lin, Y., & Bao, X. (2022). A source of WRF simulation error for the early-summer warm-sector heavy rainfall over South China coast: Land-sea thermal contrast in the boundary layer. *Journal of Geophysical Research: Atmospheres*, *127*(4), e2021JD035179. https://doi.org/10.1029/2021JD035179

Groff, F. P., Adams-Selin, R. D., & Schumacher, R. S. (2021). Response of MCS low-frequency gravity waves to vertical wind shear and nocturnal thermodynamic environments. *Journal of the Atmospheric Sciences*, *78*(12), 3889–3908. https://doi.org/10.1175/JAS-D-20-0208.1

Han, B., Du, Y., Wu, C., & Liu, X. (2021). Microphysical characteristics of the coexisting frontal and warm-sector heavy rainfall in South China. *Journal of Geophysical Research: Atmospheres*, *126*(21), e2021JD035446. https://doi.org/10.1029/2021JD035446

Hong, S.-Y., Noh, Y., & Dudhia, J. (2006). A new vertical diffusion package with an explicit treatment of entrainment processes. *Monthly Weather Review*, *134*(9), 2318–2341. https://doi.org/10.1175/MWR3199.1

Huang, L., & Luo, Y. (2017). Evaluation of quantitative precipitation forecasts by TIGGE ensembles for South China during the presummer rainy season. *Journal of Geophysical Research: Atmospheres*, *122*(16), 8494–8516. https://doi.org/10.1002/2017JD026512

Huang, S. (1986). *Heavy rainfall over southern China in the presummer rainy season (in Chinese)*. Guangdong Science and Technology Press.

Iacono, M. J., Delamere, J. S., Mlawer, E. J., Shephard, M. W., Clough, S. A., & Collins, W. D. (2008). Radiative forcing by long-lived greenhouse gases: Calculations with the AER radiative transfer models. *Journal of Geophysical Research*, *113*(D13), 2008JD009944. https://doi.org/10.1029/2008JD009944

Jiménez, P. A., Dudhia, J., González-Rouco, J. F., Navarro, J., Montávez, J. P., & García-Bustamante, E. (2012). A revised scheme for the WRF surface layer formulation. *Monthly Weather Review*, *140*(3), 898–918. https://doi.org/10.1175/MWR-D-11-00056.1

Kain, J. S. (2004). The Kain–Fritsch convective parameterization: An update. *Journal of Applied Meteorology*, *43*(1), 170–181. https://doi.org/10.1175/1520-0450(2004)043<0170:TKCPAU>2.0.CO;2

Lane, T. P. (2021). Does lower-stratospheric shear influence the mesoscale organization of convection? *Geophysical Research Letters*, *48*(3), e2020GL091025. https://doi.org/10.1029/2020GL091025

Lane, T. P., & Reeder, M. J. (2001). Convectively generated gravity waves and their effect on the cloud environment. *Journal of the Atmospheric Sciences*, *58*(16), 2427–2440. https://doi.org/10.1175/1520-0469(2001)058<2427:CGGWAT>2.0.CO;2

Liu, X., Luo, Y., Huang, L., Zhang, D., & Guan, Z. (2020). Roles of double low-level jets in the generation of coexisting inland and coastal heavy rainfall over South China during the presummer rainy season. *Journal of Geophysical Research: Atmospheres*, *125*(18), e2020JD032890. https://doi.org/10.1029/2020JD032890

Livneh, B., Restrepo, P. J., & Lettenmaier, D. P. (2011). Development of a unified land model for prediction of surface hydrology and land–atmosphere interactions. *Journal of Hydrometeorology*, *12*(6), 1299–1320. https://doi.org/10.1175/2011JHM1361.1

Luo, Y., Zhang, R., Wan, Q., Wang, B., Wong, W. K., Hu, Z., et al. (2017). The southern China monsoon rainfall experiment (SCMREX). *Bulletin of the American Meteorological Society*, *98*(5), 999–1013. https://doi.org/10.1175/BAMS-D-15-00235.1

Mapes, B. E. (1993). Gregarious tropical convection. *Journal of the Atmospheric Sciences*, *50*(13), 2026–2037. https://doi.org/10.1175/1520-0469(1993)050<2026:GTC>2.0.CO;2

NCEP. (2000). NCEP FNL operational model global tropospheric analyses, continuing from July 1999 (updated daily). [Dataset]. *Research Data Archive at the National Center for Atmospheric Research, Computational and Information Systems Laboratory*. https://doi.org/10.5065/D6M043C6

Nicholls, M. E., Pielke, R. A., & Cotton, W. R. (1991). Thermally forced gravity waves in an atmosphere at rest. *Journal of the Atmospheric Sciences*, *48*(16), 1869–1884. https://doi.org/10.1175/1520-0469(1991)048<1869:TFGWIA>2.0.CO;2

Rao, X., Zhu, K., Zhao, K., Chen, X., Hu, S., Liu, X., & Zhou, A. (2023). Evaluation and error source analysis of convection-permitting forecasts for localized nocturnal rainfall over a complex mountainous region in Pearl River Delta, South China. *Journal of Geophysical Research: Atmospheres*, *128*(21), e2023JD039065. https://doi.org/10.1029/2023JD039065

Skamarock, W. C., Klemp, J. B., Dudhia, J., Gill, D. O., Liu, Z., Berner, J., et al. (2019). A description of the advanced research WRF model version 4. NCAR Technical Note NCAR/TN-556+STR.145.

Stephan, C. C., Alexander, M. J., Hedlin, M., de Groot-Hedlin, C. D., & Hoffmann, L. (2016). A case study on the far-field properties of propagating tropospheric gravity waves. *Monthly Weather Review*, *144*(8), 2947–2961. https://doi.org/10.1175/MWR-D-16-0054.1

Su, L., Sun, X., Du, Y., Fung, J. C. H., & Chen, G. (2023). The roles of local convergences in the convection initiation of a record-breaking rainfall event at the coastal pearl river delta in South China. *Journal of Geophysical Research: Atmospheres*, *128*(3), e2022JD037234. https://doi.org/10.1029/2022JD037234

Sun, X., Luo, Y., Gao, X., Wu, M., Li, M., Huang, L., et al. (2021). On the localized extreme rainfall over the great bay area in South China with complex topography and strong UHI effects. *Monthly Weather Review*, *149*(8), 2777–2801. https://doi.org/10.1175/MWR-D-21-0004.1

Thompson, G., Field, P. R., Rasmussen, R. M., & Hall, W. D. (2008). Explicit forecasts of winter precipitation using an improved bulk microphysics scheme. Part II: Implementation of a new snow parameterization. *Monthly Weather Review*, *136*(12), 5095–5115. https://doi.org/10.1175/2008MWR2387.1

Wang, H., Luo, Y., & Jou, B. J. (2014). Initiation, maintenance, and properties of convection in an extreme rainfall event during SCMREX: Observational analysis. *Journal of Geophysical Research: Atmospheres*, *119*(23). https://doi.org/10.1002/2014JD022339

Wu, M., & Luo, Y. (2016). Mesoscale observational analysis of lifting mechanism of a warm-sector convective system producing the maximal daily precipitation in China mainland during pre-summer rainy season of 2015. *Journal of Meteorological Research*, *30*(5), 719–736. https://doi.org/10.1007/s13351-016-6089-8

Wu, N., Zhuang, X., Min, J., & Meng, Z. (2020a). Practical and intrinsic predictability of a warm-sector torrential rainfall event in the South China monsoon region. *Journal of Geophysical Research: Atmospheres*, *125*(4), e2019JD031313. https://doi.org/10.1029/2019JD031313

Wu, Y., Liu, Z., & Li, D. (2020b). Improving forecasts of a record-breaking rainstorm in Guangzhou by assimilating every 10-min AHI radiances with WRF 4DVAR. *Atmospheric Research*, *239*, 104912. https://doi.org/10.1016/j.atmosres.2020.104912

Xie, P., Joyce, R., Wu, S., Yoo, S., Yarosh, Y., Sun, F., et al. (2018). NOAA climate data record (CDR) of CPC morphing technique (CMORPH) high resolution global precipitation estimates, version 1 [Dataset]. *NOAA National Centers for Environmental Information*. https://doi.org/10.25921/W9VA-Q159

Yang, H. (2023). WRF simulation with latent heating rate output [Dataset]. *Zenodo*. https://doi.org/10.5281/ZENODO.10183294

Yang, H., & Du, Y. (2024). Difference between upshear- and downshear-propagating waves associated with the development of squall lines. *Monthly Weather Review*, *152*(6), 1399–1420. https://doi.org/10.1175/MWR-D-23-0109.1

Yang, H., Du, Y., & Wei, J. (2023). Generation of multiple gravity wave couplets from convection. *Journal of the Atmospheric Sciences*, *80*(9), 2323–2343. https://doi.org/10.1175/JAS-D-22-0212.1

Zeng, Z., Huang, L., Schultz, D. M., Garcia-Carreras, L., & Wang, D. (2023). Comparing synoptic conditions and environmental characteristics for fronts with and without prefrontal convection initiation and heavy rain over coastal South China. *Monthly Weather Review*, *151*(12), 3235–3254. https://doi.org/10.1175/MWR-D-23-0054.1

Zhang, M., & Meng, Z. (2019). Warm-sector heavy rainfall in southern China and its WRF simulation evaluation: A low-level-jet perspective. *Monthly Weather Review*, *147*(12), 4461–4480. https://doi.org/10.1175/MWR-D-19-0110.1

Zhang, M., Rasmussen, K. L., Meng, Z., & Huang, Y. (2022). Impacts of coastal terrain on warm-sector heavy-rain-producing MCSs in southern China. *Monthly Weather Review*, *150*(3), 603–624. https://doi.org/10.1175/MWR-D-21-0190.1

Zhang, S., Liang, Z., Wang, D., & Chen, G. (2022). Nocturnal convection initiation over inland South China during a record-breaking heavy rainfall event. *Monthly Weather Review*, *150*(11), 2935–2957. https://doi.org/10.1175/MWR-D-21-0264.1